Nanoscale

Exploring the effect of nanocrystal facet orientations in g-C3N4/BiOCl heterostructures on photocatalytic performance

Journal:	*Nanoscale*
Manuscript ID	NR-ART-07-2015-005154.R1
Article Type:	Paper
Date Submitted by the Author:	22-Sep-2015

Complete List of Authors:	Li, Qingbo; Shandong University, School of Chemistry and Chemical Engineering Zhao, Xian; State Key Laboratory of Crystal Materials, Shandong University Yang, Jun; Institute of Process Engineering, Chinese Academy of Sciences, Group of Materials for Energy Conversion and Environmental Remediation (MECER) Jia, Chun-Jiang; Shandong University, School of Chemistry and Chemical Engineering Jin, Zhao; Shandong University, Chemistry and Chemical Engineering Fan, Weiliu; Shandong University, School of Chemistry and Chemical Engineering

Nanoscale

ARTICLE

Exploring the effect of nanocrystal facet orientations in g-C_3N_4/BiOCl heterostructures on photocatalytic performance

Received 00th January 20xx,
Accepted 00th January 20xx

DOI: 10.1039/x0xx00000x

www.rsc.org/

Qingbo Li[a], Xian Zhao[b], Jun Yang[c], Chun-Jiang Jia[a], Zhao Jin[a] and Weiliu Fan[a]*

Effective separation and migration of photogenerated electron–hole pairs are two key factors to determine the performance of photocatalysts. It has been widely accepted that photocatalysts with heterojunctions usually exhibit excellent charge separation. However, the migration process of separated charges in heterojunction structures has not been fully investigated. Herein, photocatalysts with heterojunctions are constructed by loading g-C_3N_4 nanoparticles onto the BiOCl nanosheets with different exposed facets (BOC-001 and BOC-010). The g-C_3N_4 nanoparticles with decreasing size and increasing zeta potential could induce stronger coupling and scattering in the heterojunction. The relationship between the crystal facet orientation in the BiOCl nanosheets and the charge separation/effective migration behaviours of the materials is investigated. The visible light photocatalytic activity of the composites is evaluated by methyl orange (MO) and phenol degradation experiments, and the results show that ng-CN/BOC-010 composites exhibit higher photocatalytic performance than that of ng-CN/BOC-001 composites. Both photoelectrochemical and fluorescence emission measurements indicate that the different exposed facets in ng-CN/BiOCl composites could induce the migration of the photogenerated electrons in different ways, but do not significantly alter the separation efficiencies. The separated electrons in ng-CN/BOC-010 undergo a shorter transport distance than that of ng-CN/BOC-001 to reach the surface reactive sites. The study may suggest that the crystal facet orientation in polar semiconductors is a critical factor for designing highly efficient heterojunction photocatalysts.

KEYWORDS: crystal facet orientation, heterojunction, polar semiconductor, charge separation and migration

Introduction

Constructing effective heterojunctions is a promising approach for enhancing photocatalytic activity by increasing the charge separation efficiency.[1-7] The difference in the chemical potentials between the different components induces a built-in field, which promotes the spatial separation of electron-hole pairs on different sides of the heterojunction.[4-6] Many studies have been devoted to the development of new heterostructures and the control of band edge alignment in order to improve photocatalytic performance.[8, 9] However, the separated charges (electrons and holes) may suffer from being confined to one component of the heterojunction, as they may not be easily accessible for the surface reaction. Thus, in addition to the effective separation of the electrons and holes, the efficient transfer of the separated electrons/holes from the bulk of the photocatalyst to the outer surface also remains a challenge in the development of heterostructured photocatalysts with high-performance. To address this issue, particular attention should be paid to the utilization of the benefits offered by the constituent phases. In addition to energy level match, the two correlated components must exhibit complementary spectral sensitivity to maximize migration efficiency of the separated charges in single phase operation. It is accepted that enhanced photocatalytic activity can be achieved by utilizing the internal electric field of polar semiconductors.[10, 11] Jiang et al. reported that the internal bias electric field along the b axis in $NaNbO_3$ single crystals could facilitate the separation and transportation of electron-hole pairs.[11] Also, the internal field created by polar surface termination in $SrTiO_3$ structures can promote the separation of photogenerated charge carriers and facilitate spatially selective oxidation and reduction.[12] Thus, in order to achieve optimum overall performance, an alternative strategy is employing an additional electric field to promote the spatial migration of electrons and holes. In this case, the coupling and relative orientation of the two internal electric fields are the key factors.

[a] Key Laboratory for Colloid and Interface Chemistry of State Educating Ministry, School of Chemistry and Chemical Engineering, Shandong University, Jinan 250100, China. Fax: +86-531-88364864; Tel: +86-531-88366330; E-mail: fwl@sdu.edu.cn
[b] State Key Laboratory of Crystal Materials, Shandong University, Jinan 250100, China
[c] State Key Laboratory of Multiphase Complex Systems, Institute of Process Engineering, Chinese Academy of Sciences, Beijing, 100190, China

† Electronic Supplementary Information (ESI) available: Microscopic images, SAED patterns, XRD patterns, FT-IR spectra, UV-Vis spectra, photocatalytic evaluation, VB XPS spectra, and additional table for the characterization of the materials in this study. See DOI: 10.1039/x0xx00000x

Recently, bismuth oxychloride (BiOCl) has attracted increasing research interest due to its broad range of applications.[13-16] BiOCl has a layered structure in the [001] direction, which provides enough space to polarize the proximal atoms and orbitals and induces internal static electric fields.[17-21] Zhang et al. achieved the facet-controllable synthesis of BiOCl single-crystalline nanosheets, and found that BOC-001 has higher activity under UV radiation compared to BOC-010, owing to the more suitable internal electric fields in the [001] direction, which are beneficial for promoting the separation of charge carriers.[21] However, the band gap of BiOCl is about 3.5 eV, making it useful only under UV irradiation, which leads to poor photocatalytic performance under visible light.[22, 23] An effective approach to overcome this drawback is the construction of a heterojunction between BiOCl and another semiconductor with a narrow band gap, aiming to imbue BiOCl with visible light photocatalytic activity.[3, 24-27] Although several BiOCl-based heterostructures have been synthesized for visible light photocatalysis, suitable combinations of BiOCl nanosheets with specific exposed facets and other materials for high-performance photocatalysis have been rarely reported.[28] As reported by Zhang et al.,[21] the electric field in BOC-001 is perpendicular to the exposed facets, while BOC-010 has an internal electric field, which is parallel to the surface. These different crystal orientations provide an ideal platform to study the charge-migration behavior in the heterojunction.[29] BiOCl is a suitable material for investigating whether the polar electric fields in polar semiconductors is a key factor for tuning the migration process of separated charges in heterojunctions, as it possesses a strong dipole moment. This hypothesis can be justified by controlling the crystal facet orientation of BiOCl nanosheets, which determines the relative orientation between the polar internal electric field and the heterojunction interface.

Recently, graphitic carbon nitride (g-C_3N_4) has attracted extensive attention as a potential photocatalyst with excellent visible-light response due to its narrow band gap of 2.7 eV.[30] Since g-C_3N_4 possesses very high thermal and chemical stability, it can be used as a visible-light-driven photocatalyst for the photo-splitting of water and organic pollutant degradation.[31-37] However, the photocatalytic performance of g-C_3N_4 is far from optimal because of its poor mass diffusion and fast charge recombination. Fortunately, these shortcomings might be overcome through fabricating heterojunctions with other photocatalysts.[38-40]

In the case of g-C_3N_4/BiOCl composites, the favorable optical properties of g-C_3N_4 (absorption bands in the visible region) and good electrical conductivity of BiOCl nanosheets (an efficient polar electric field) make this system potentially suitable for photocatalysis using visible light. It must be noted, however, that due to the tendency of g-C_3N_4 to form irregular aggregates of stacked multilayers, the precise structural arrangement of g-C_3N_4 nanostructures on BiOCl nanosheets is difficult, and this may have negative effects on the interfacial contact. In this work, in order to overcome the aggregation problem, and, consequently, to maximize the contact between the g-C_3N_4 and BiOCl nanosheets, the preliminary exfoliation of g-C_3N_4 has been performed via ultrasonication. It is reported that an intense cavitation field can exfoliate and fragment thick bulk g-C_3N_4 to nanoparticles in the 70-160 nm size range.[41] After ultracentrifugation, the suspension containing g-C_3N_4 nanoparticles can then be used to impregnate BiOCl nanosheets.

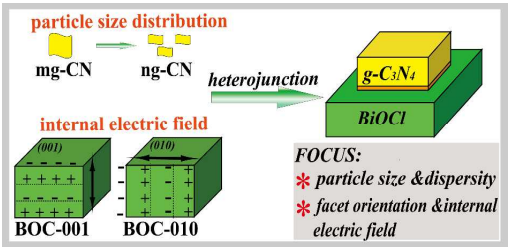

Fig. 1 Schematic illustration to show the construction of efficient heterojunction photocatalysts in this work.

In this study, size-controlled g-C_3N_4 was composited with different exposed facets of BiOCl (BOC-001 and BOC-010). The photocatalytic and photoelectrochemical performances of the materials were investigated and compared thoroughly. We mainly focused on two factors to construct efficient heterojunction photocatalysts: the structure, dispersion, and optical properties of the g-C_3N_4 nanoparticles, and the influence of the crystal facet orientation of the BiOCl nanosheets on the migration of separated charge carriers. The overall research concept is schematically illustrated in Fig. 1. The mechanism understanding might be helpful for designing heterojunction photocatalysts with high efficiency.

Experimental

Synthesis of g-C_3N_4 samples

All starting materials were reagent grade and used without further purification. The microsized g-C_3N_4 (mg-CN) was prepared by the polymerization of melamine molecules under high temperatures.[36] In detail, melamine was heated at a rate of 20°C min^{-1} to 550°C, and maintained at this temperature for 2 h. Then further deammoniation was performed at 550 °C for 2 h. The obtained yellow product was mg-CN powder. Nanosized g-C_3N_4 (ng-CN) was obtained by liquid exfoliation of the as-prepared mg-CN in water.[41] An appropriate amount of mg-CN powder was dispersed in water and ultrasonicated at 35 KHz for ca. 12 h. The obtained yellow turbid suspension was then centrifuged at 5000 rpm for 5 min to remove the larger mg-CN particles. The separated suspension was then centrifuged at 12,000 rpm to obtain ng-CN. A sample of mixed microsized g-C_3N_4 and nanosized g-C_3N_4 (mng-CN) was obtained by directly centrifuging the yellow turbid suspension at 12,000 rpm (i.e. without the first centrifugation process).

Synthesis of BiOCl with exposed (001) and (010) facets

BiOCl nanosheets were synthesized by a hydrothermal method described previously.[21] In detail, 1 mmol of $Bi(NO_3)_3{\cdot}5H_2O$ and 1 mmol of KCl were added to 15 mL of distilled water at room temperature with continuous stirring, and then 1 M NaOH solution was added to adjust the pH value of the solution to 6.0.

The mixture was stirred for 30 min and then decanted into a 20-mL autoclave with an inner Teflon lining. The autoclave was heated at 160 °C for 24 h under autogenous pressure, and then cooled down to room temperature naturally. The resulting precipitates were collected, thoroughly washed with deionized water and ethanol, and dried at 60 °C. The obtained sample was designated BOC-010. BOC-001 was obtained under the same conditions but without the addition of NaOH.

Synthesis of g-C_3N_4/BiOCl composites

An appropriate amount of ng-, mg-, or mng-CN was added to 15 mL of water, and the beaker was placed in an ultrasonic bath for 30 min to completely disperse the powder. Then, an appropriate amount of BOC-001 or BOC-010 powder was added to the above suspension and stirred in a fume-hood for 24 h. The resultant samples were dried at 60 °C and calcined at 250 °C for 3 h. According to this method, ng-CN/BOC-010, mg-CN/BOC-001, mg-CN/BOC-010, mng-CN/BOC-001, and mng-CN/BOC-010 composites were synthesized.

Characterization

Scanning electron microscopy (SEM) images were obtained on an S-4800 field emission SEM (FESEM, Hitachi, Japan). Transmission electron microscopy (TEM) and high-resolution TEM (HRTEM) analyses were conducted using a JEM 2100 microscope at an accelerating voltage of 200 kV. Zeta potentials of 0.5 mg mL^{-1} nanoparticle suspensions were obtained from phase analysis light-scattering measurements performed on a ZetaPALS instrument. Powder X-ray diffraction (XRD) patterns were recorded on a D8 Advance X-ray diffractometer (Bruker, Germany) with Cu-Kα radiation operated in a 2θ range of 10°–80° with a step width of 0.02°. Fourier transform infrared (FT-IR) spectra were recorded on a NEXUS 670 infrared spectrometer. X-ray photoelectron spectroscopy (XPS) and valence band X-ray photoelectron spectroscopy (VB XPS) of the samples were performed on an ESCALAB 250 spectrometer equipped with an Al Kα source, and the binding energies of the composing elements were referenced to the C 1s peak at 284.6 eV. Ultraviolet visible (UV-Vis) diffuse reflectance spectroscopies (DRS) were measured using a UV-Vis spectrophotometer (Shimadzu UV-2550, Japan) and $BaSO_4$ as the reflectance standard. A Builder 4200 instrument was used to measure the Brunauer–Emmett–Teller (BET) surface areas of the samples at liquid nitrogen temperature. The fluorescence emission spectra were obtained using a luminescence spectrophotometer (Hitachi F-4500) operated at room temperature.

Photocatalytic experiments

Photocatalytic activities of the as-prepared samples were evaluated by the degradation of methyl orange (MO) and phenol under visible-light irradiation using a 300 W metal-halide lamp with a 420 nm cut-off filter as the light source. In detail, 30 mg of photocatalyst was dispersed in 50 mL of MO (20 mg L^{-1}) and phenol (30 mg L^{-1}) solution and the suspension was continuously stirred in the dark for 30 min to reach the adsorption/desorption equilibrium between the photocatalyst and the degrading pollutants. During the degradation, the reaction solution was sampled at specific time-points and centrifuged to remove photocatalysts in order to monitor the intensity changes of the absorption peaks at 463 nm and 270 nm using a Hitachi U-3500 UV-vis spectrometer, which were used to determine the concentration of the MO and phenol at different times.

Active species trapping experiments

To detect the active species during the photocatalytic reaction, 1 mmol of a hole scavenger (triethanolamine, TEOA), electron scavenger ($AgNO_3$), superoxide radical anion scavenger (benzoquinone, BQ), or hydroxyl radical scavenger (tert-butyl alcohol, TBA) was added to the MO solution. Otherwise, the method was similar to the photocatalytic experiment described above.

Photoelectrochemical measurements

The photocurrents and electrochemical impedance spectroscopy (EIS) experiments were carried out on an electrochemical workstation (LAN-LIKE, Tianjin, China) using a standard three-electrode system with the samples as the working electrodes, a Pt foil as the counter electrode, and Ag/AgCl (saturated KCl) as the reference electrode, respectively. For the fabrication of the working electrodes, 50 mg of the products were dispersed in a certain amount of ethanol and Nafion solution homogeneously under sonication for 10 min. The as-prepared samples were spread on a tin oxide conducting glass (area of 0.25 cm^2) and allowed to dry under ambient conditions. The electrodes were immersed in Na_2SO_4 aqueous solution (0.5 M) with or without $K_2S_2O_8$ (0.1 M) and irradiated by a 300 W Xe arc lamp (PLS-SXE300C/300CUV, Beijing Trusttech Co., Ltd.) with a 420 nm cut-off filter. The photocurrents with light on and off were measured at 0.5 V. EIS was conducted over a frequency range of 10 mHz−100 kHz.

Results and discussion

Structure and morphology of g-C_3N_4/BiOCl heterojunction photocatalysts

The morphologies and detailed structural features of pure BiOCl nanosheets were investigated with SEM and TEM, as shown by Fig. S1 of the Electronic Supplementray Information (ESI). The results demonstrate that BiOCl nanosheets with exposed {001} and {010} facets were selectively synthesized, which is consistent with a previous report.[21] The morphologies of the as-prepared g-C_3N_4 and g-C_3N_4/BiOCl composites are shown by the SEM images in Fig. 2. As displayed by Fig. $2a_0$, the mg-CN exhibits a typically aggregated morphology with a large particle size of several micrometers and lamellar structure, whereas the ng-CN obtained by sonication exhibits small particles with a size of 100−500 nm and good dispersity (Fig. $2c_0$). Fig. $2b_0$ shows that mng-CN is composed of mg-CN and ng-CN. Also, as revealed by Fig. $2a_1$ and Fig. $2a_2$, the mg-CN does not effectively integrate with BOC-001 or BOC-010, but aggregates significantly, whereas the ng-CN is uniformly deposited on the BiOCl surface (Fig. $2c_1$ and Fig. $2c_2$,). This phenomenon is more obvious in the mng-CN/BOC composites. As shown in Fig. $2b_1$ and Fig. $2b_2$, ng-CN is deposited on the surface of BiOCl, whereas mg-CN aggregates at other places. Therefore, the small ng-CN nano-islands are uniformly formed on the surface of BiOCl and tend to construct more effective heterojunction interfaces,

providing a potential advantage for the enhancement of charge separation, and, thus, for the improvement of photocatalytic performance.

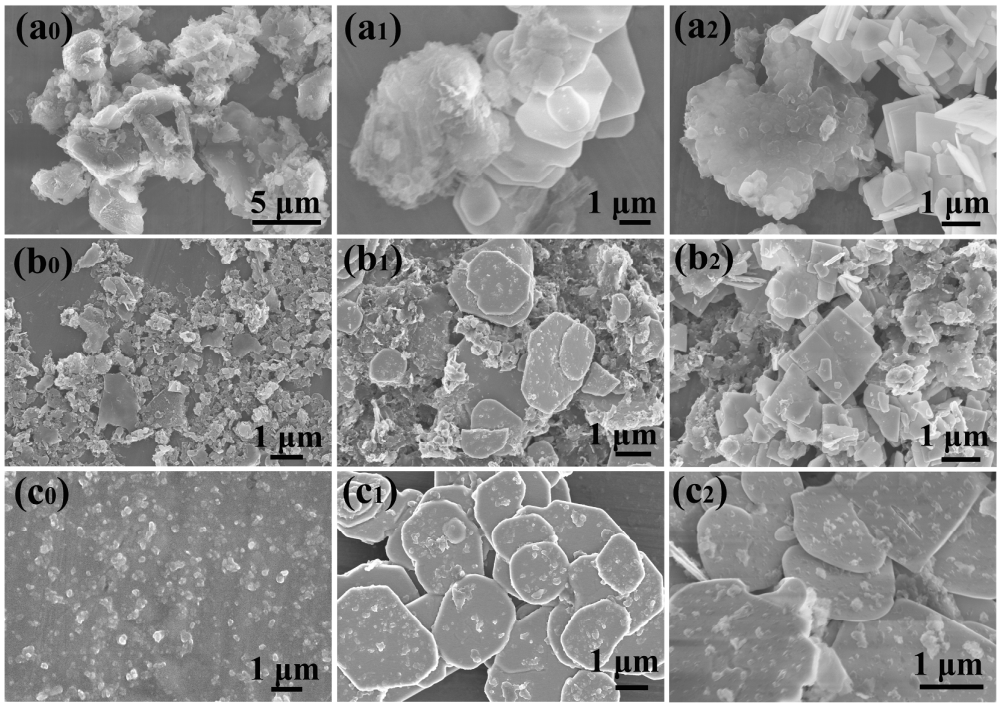

Fig. 2 SEM images of as-prepared samples: (a_0) mg-CN, (a_1) mg-CN/BOC-001, (a_2) mg-CN/BOC-010, (b_0) mng-CN, (b_1) mng-CN/BOC-001, (b_2) mng-CN/BOC-010, (c_0) ng-CN, (c_1) ng-CN/BOC-001, (c_2) ng-CN/BOC-010.

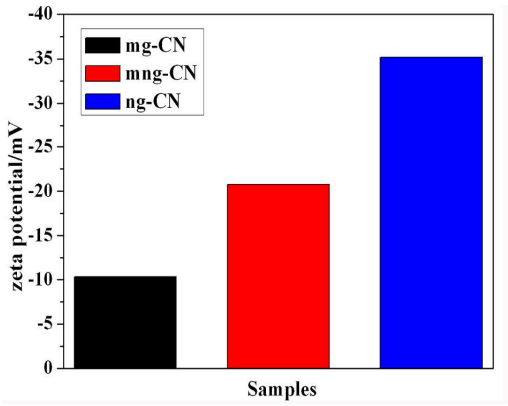

Fig. 3 Zeta potentials of mg-CN, mng-CN, and ng-CN.

Fig. 3 shows zeta potential measurements for the as-prepared g-C_3N_4 samples. The zeta potential (ζ) is a key parameter in determining the stability of nanoparticles in dispersion. In general, particles in dispersion are electrically stabilized with zeta potentials of ζ < −30 mV or > +30 mV, while they tend to aggregate as the zeta potential approaches to zero. Therefore, ng-CN has good dispersity and stability in an aqueous system, with a zeta potential of ca. -35.15 mV. This is consistent with a previous report by Zhang et al.[41] Conversely, the zeta potential of mg-CN is -10.35 mV, indicating that mg-CN is not stable in aqueous solution. The influence of particle size on zeta potential was confirmed by experiment, which shows that zeta potential decreases with increasing particle size. In general, the ratio of surface-exposed atoms increases with the decrease of particle size, and hence small nanoparticles have higher mean bond energy per atom. Also, more vacancies occur on the surfaces because atoms/ions tend to leach from the surface, thus increasing the surface charge.[42]

The formation process is depicted schematically in Fig. 4. mg-CN tends to aggregate in the beaker bottom where it cannot form heterostructures with BiOCl, whereas ng-CN is uniformly dispersed in water, favorable for uniform deposition onto the BiOCl surfaces. From another perspective, the most likely growth process during the mechanically mixed procedure is related to oriented attachment resulting from collision-induced heteroaggregation.[43, 44] Effective collision occurs more easily between a smaller particle with high mobility and a larger particle with a large collision cross section.[45] Thus, the formation of heterojunctions is more easily achieved between large BiOCl nanosheets and ng-CN nanoparticles, whereas the possibility for the mg-CN/BOC heterojunction formation is low because effective collisions rarely occur between two large species.

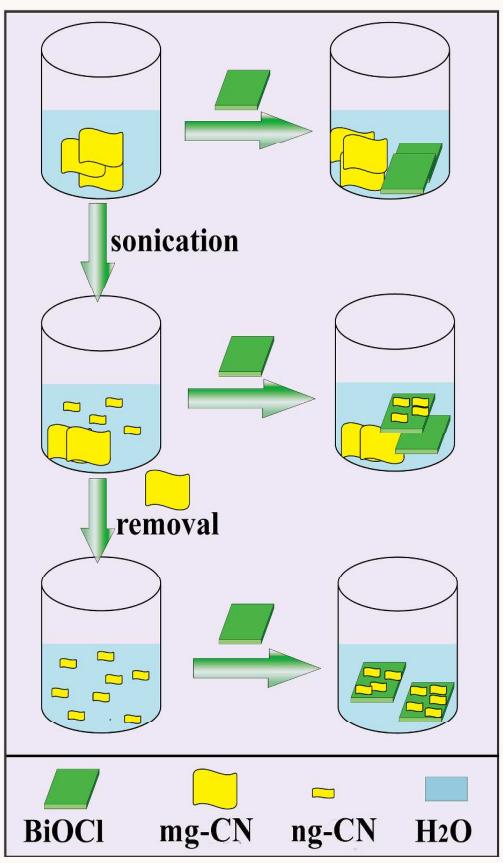

Fig. 4 Schematic illustration to depict the preparation of mg-CN/BiOCl, mng-CN/BiOCl, and ng-CN/BiOCl.

Further detailed structural information of ng-CN/BiOCl heterojunction photocatalysts was obtained using TEM and high-resolution TEM (HRTEM), as exhibited in Fig. 5. For ng-CN/BiOCl heterojunction photocatalysts, ng-CN (marked by orange circles) covers the BiOCl surfaces (Fig. 5a_1 and Fig. 5b_1). The ng-CN is not obvious in the TEM images because of the large thickness of BiOCl. HRTEM analysis, as defined by the red square (Fig. 5a_2), clearly indicates the presence of (110) planes with a lattice spacing of 0.275 nm. The angle indicated by the corresponding selected-area electron diffraction (SAED) pattern (Fig. 5a_3) is 45°, which is identical to the theoretical value of the angle between (110) and (200) faces. The set of diffraction spots can be indexed as the [001] zone axis of BiOCl. It is apparent that the introduction of ng-CN has no effect on the crystallinity of BOC-001. By contrast, in the ng-CN/BOC-010 sample, the angle labeled in the SAED pattern, and indexed as the [010] zone, is 43.4°, which is in good agreement with the theoretical value of the angle between (102) and (002) (Fig. 5b_3). BOC-001 maintains good crystallinity after composition with ng-CN. The lattice fringes of 0.37 nm correspond to the (002) atomic planes (Fig. 5b_2). These results indicate that the ng-CN/BiOCl heterojunctions are composed of ng-CN and BiOCl, and that the main exposed facets of BiOCl in the two ng-CN/BiOCl samples are {001} and {010}, respectively.

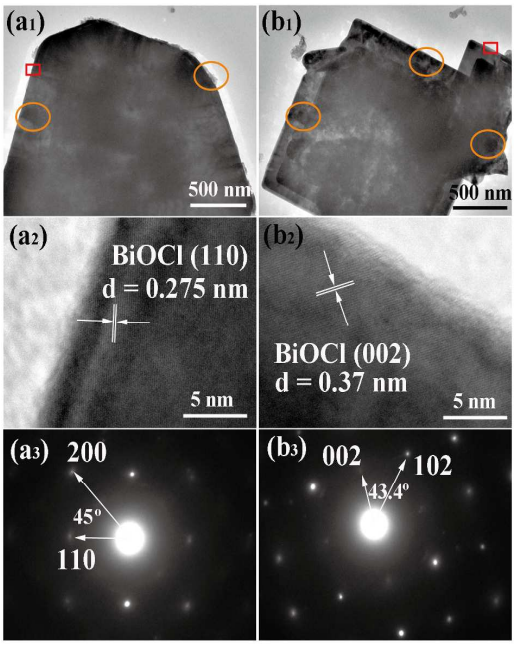

Fig. 5 (a_1,b_1) TEM images, (a_2,b_2) SAED patterns, and (a_3,b_3) HRTEM images of ng-CN/BOC-001 and ng-CN/BOC-010.

The XRD patterns of pure BiOCl, ng-CN, and ng-CN/BiOCl heterojunction photocatalysts are shown in Fig. 6a. The diffraction peaks of BiOCl nanosheets could be indexed as tetragonal-phase BiOCl (by reference to JCPDS No. 06-0249). The intensity ratio of the (002) and (101) peaks in BOC-001 differs from that of BOC-010, indicating that the surfaces of the two samples are different. This result is consistent with the above-mentioned HRTEM analysis. The ng-CN displays two peaks at 13.1° and 27.5°. The peak originating from the periodic stacking of layers in the nanosheets is at 27.5°, and the low-angle reflection peak at 13.1° corresponds to the interlayer structural packing. A comparison of the XRD patterns of mg-CN and mng-CN (ESI Fig. S2a) shows that the ng-CN has basically the same crystal structure as its parent mg-CN. The low-angle reflection peak at 13.1° is weaker in the ng-CN pattern. A similar change is also observed in the g-C_3N_4 nanoparticles and nanosheets, which is attributed to the decreased planar size of g-C_3N_4.[46, 47] After compositing with ng-CN, ng-CN/BiOCl heterojunction photocatalysts are well crystallized and show no apparent changes, indicating the preservation of the basic BiOCl phase structure. The typical pattern for ng-CN (002) is observed in the ng-CN/BiOCl heterojunction photocatalyst. Thus, the heterojunction samples have a two-phase composition: ng-CN and BiOCl. The XRD patterns of mng-CN/BiOCl and mg-CN/BiOCl samples are basically same as those of ng-CN/BiOCl heterojunction photocatalysts (ESI Fig. S2a).

Fig. 6b shows the FT-IR spectra of pure BiOCl, ng-CN, and the ng-CN/BiOCl heterojunction photocatalysts. The IR spectrum of ng-CN shows almost identical absorption bands as those of the bulk mg-CN (ESI Fig. S2b), indicating that the ng-CN retains the same crystal structure as that of mg-CN. The

sharp peak centered at 814 cm^{-1} originates from the vibration of the triazine ring.[30] The absorption bands between 1000 cm^{-1} and 1800 cm^{-1} correspond to either trigonal C–N(–C)–C (full condensation) or bridging C–NH–C units.[30, 48] The absorption band at 528 cm^{-1} (539 cm^{-1}) is assigned as the Bi-O stretching mode.[48, 49] The slight difference between BOC-001 and BOC-010 is attributed to the different surface structures of the samples. All the bands are present in the spectra of the ng-CN/BiOCl heterojunction photocatalysts, which suggest that the heterojunctions contain the two fundamental components, i.e. BiOCl and ng-CN.

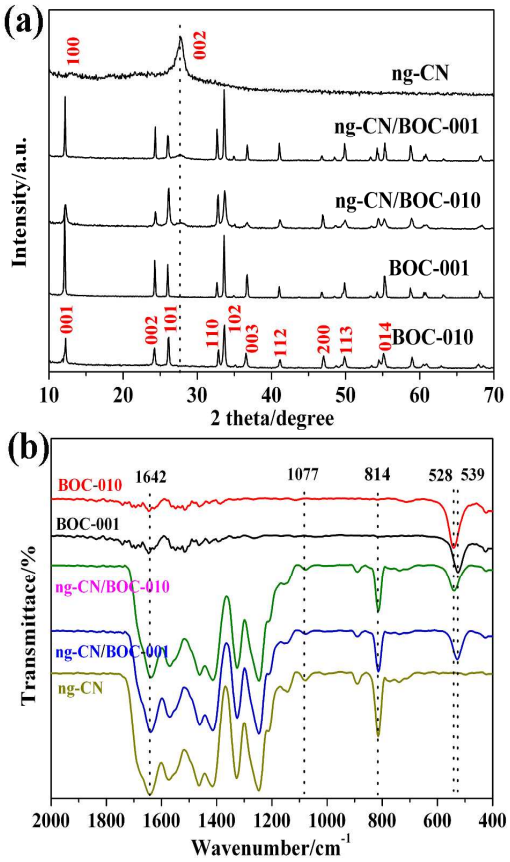

Fig. 6 (a) XRD patterns and (b) FT-IR spectra of ng-CN, BiOCl, and ng-CN/BiOCl heterojunction photocatalysts.

XPS was conducted to characterize the composition and chemical status of the elements in the ng-CN/BiOCl heterojunction photocatalysts compared to those of pure ng-CN and BiOCl. The XPS spectra in Fig. 7a show that the ng-CN/BiOCl heterojunction photocatalysts consist of Bi, O, C, Cl, and N. The high-resolution Bi 4f, Cl 2p, O 1s, C 1s, and N 1s spectra are shown in Fig. 7b-f. The two strong peaks in pure BOC-001 at 159.0 and 164.2 eV are attributed to Bi $4f_{7/2}$ and Bi $4f_{5/2}$, respectively, which are characteristics of Bi^{3+} species in a BiOCl network.[24] Peaks with binding energies of 198.3 and 199.9 eV correspond to Cl $2p_{3/2}$ and Cl $2p_{1/2}$, respectively, for BOC-001 (Fig. 6c).[50] The O 1s core level spectrum of BOC-001 shown in Fig. 6d can be fitted well with two peaks at 530.3 and 532.2 eV, relating to O^{2-} from a Bi–O bond and chemisorbed H_2O molecules or OH^- groups on the surface, respectively.[50] The binding energies of Bi $4f_{7/2}$, Bi $4f_{5/2}$, Cl $2p_{3/2}$, Cl $2p_{1/2}$, and O 1s for pure BOC-010 are the same as those of BOC-001. However, the binding energies of Bi $4f_{7/2}$ and Bi $4f_{5/2}$ for the ng-CN/BOC-001 heterojunction photocatalysts are 158.7 and 163.9 eV, respectively, both of which show a shift of 0.3 eV to lower energy compared with those of pure BOC-001. Compared with pure BOC-001, the O 1s and Cl 2p peaks of ng-CN/BOC-001 have obvious shifts ca. 0.3 eV to lower binding energies. However, the Bi 4f, Cl 2p, and O 1s peaks of the ng-CN/BOC-010 heterojunction photocatalysts show slight shifts of ca. 0.1 eV to lower binding energies compared to BOC-010, which indicates that the interfacial interaction between ng-CN and BOC-001 is stronger than that of the ng-CN/BOC-010 system. In the spectra of pure ng-CN, C1s peaks centered at 284.6 eV (C1) and 288.0 eV (C2) are ascribed to graphitic carbon on the surface of ng-CN and N=C-N groups of triazine rings, respectively (Fig. 7e).[51] The XPS N 1s peak is centered at 399.1 eV (Fig. 7f). Compared with pure ng-CN, the N 1s peaks of the ng-CN/BOC-001 and ng-CN/BOC-010 heterojunction photocatalysts show a 0.2 and 0.1 eV shift to high binding energies, respectively. The XPS spectra reveal the existence of chemical bonds between ng-CN and BiOCl in the heterojunctions, and that the interfacial interaction between ng-CN and BOC-001 is stronger than that in the ng-CN/BOC-010 system.

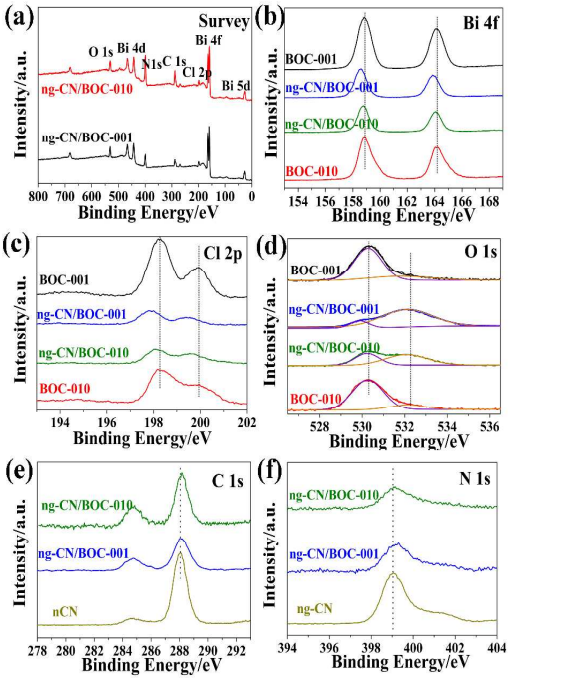

Fig. 7 (a) XPS of ng-CN/BOC-001 and ng-CN/BOC-010; (b) Bi 4f of pure BiOCl and ng-CN/BiOCl, (c) Cl 2p of pure BiOCl and ng-CN/BiOCl; (d) O 1s of pure BiOCl and ng-CN/BiOCl; (e) C 1s of pure ng-CN and ng-CN/BiOCl; and (f) N 1s of pure ng-CN and ng-CN/BiOCl heterojunction photocatalysts.

UV-vis DRS was measured to analyze the optical absorption of pure BiOCl, ng-CN, and ng-CN/BiOCl heterojunction photocatalysts, as shown in Fig. 8. The BOC-001 and BOC-010 samples have very close absorption edges in the UV region of 364 nm and 362 nm, respectively, which is in agreement with results reported elsewhere in the literature.[21] As is evident in the figure, the intrinsic absorption edge of ng-CN is 456 nm, which shows a slight blue shift in comparison with the mg-CN (absorption edge at 466 nm, ESI Fig. S2c). This blue shift of ng-CN can be ascribed to its decreased sheet size and stacking number, which can increase the intrinsic band gap by exploiting the quantum confinement effect.[52] After facet coupling, the ng-CN/BOC-001 and ng-CN/BOC-010 heterojunction photocatalysts show a similar absorption edge at 450 nm, indicating that both ng-CN/BOC-001 and ng-CN/BOC-010 heterojunction photocatalysts will exhibit good absorption of visible light.

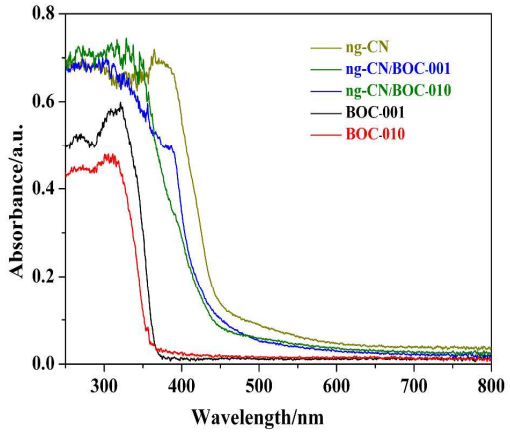

Fig. 8 UV-Vis spectra of ng-CN, BiOCl, and ng-CN/BiOCl heterojunction photocatalysts.

Photocatalytic activity of ng-CN/BiOCl heterojunction photocatalysts

The photocatalytic activities of pure ng-CN, BiOCl, and ng-CN/BiOCl composites were evaluated by decomposing MO under visible-light irradiation, as shown in Fig. 9a. Before visible-light irradiation, adsorption/desorption equilibrium between the photocatalyst and the degrading pollutants in solution was achieved. There is no obvious difference of the pollutant's concentration after dark adsorption for the ng-CN/BOC-001 and ng-CN/BOC-010 samples (ESI Fig. S3). During the degradation, unpromoted photolysis of MO is regarded as negligible. The photodegradation of MO with catalysts BOC-001 and BOC-010 was 5 % and 10.9 %, respectively, after 150 min of irradiation. The photocatalytic activity of BOC-010 under visible-light irradiation can be attributed to the indirect dye photosensitization process. The particle size of g-C3N4 has an effect on the photocatalytic activity of as-prepared g-C3N4 samples, following an order of ng-CN > mng-CN > mg-CN. The mng-CN/BiOCl and ng-CN/BiOCl heterojunction photocatalysts show dramatically enhanced photocatalytic activities compared to pure mng-CN and ng-CN.

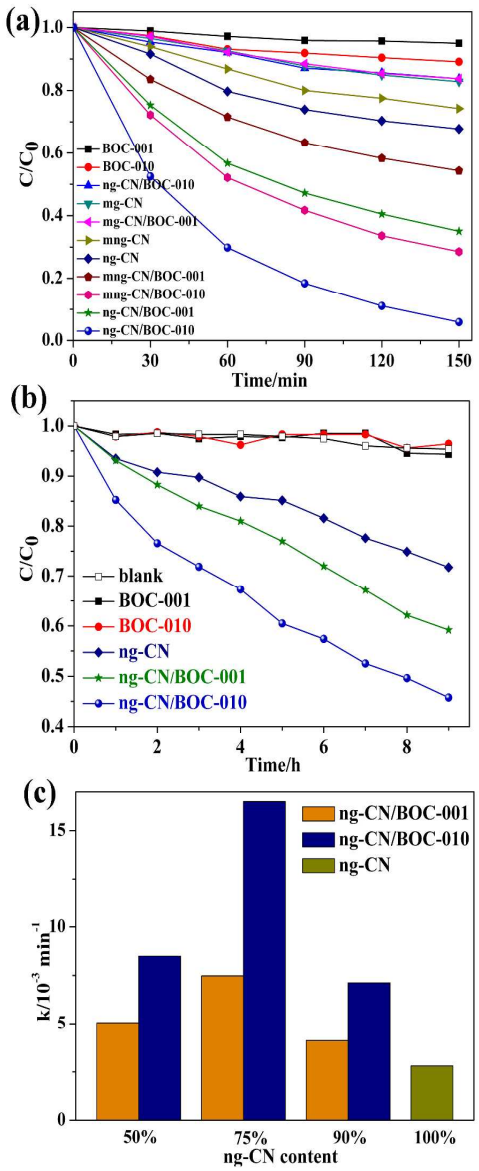

Fig. 9 (a) Photocatalytic degradation of MO over samples under visible-light irradiation. (b) Photocatalytic degradation of phenol over samples under visible-light irradiation. (c) Visible-light-induced photocatalytic degradation of MO over samples containing different proportions of ng-CN.

Also, the ng-CN/BiOCl heterojunction photocatalysts show better photocatalytic activity than that of the mng-CN/BiOCl samples. However, the photocatalytic activity of the mg-CN/BiOCl composites is not improved compared to pure mg-CN since mg-CN cannot construct efficient heterojunctions with BiOCl. This result indicates that the particle size of g-C3N4 has an influence on the formation of effective interfaces and also determines the photocatalytic performance of the composites. In addition, the ng-CN/BOC-010 heterojunction photocatalyst show higher

photocatalytic activity than the ng-CN/BOC-001 heterojunction photocatalyst, and the same trend is observed in the mng-CN/BiOCl samples. Also, the photocatalytic activity of mng-CN/BOC-010 is higher than that of ng-CN/BOC-001. This indicates that the photocatalytic activities of the heterojunction photocatalysts are mainly influenced by the exposed facets of the BiOCl nanosheets after the formation of the effective interfaces.

The experimental data were fitted by a pseudo-first-order model to quantitatively investigate reaction kinetics of MO degradation, and the corresponding apparent reaction constants (k) are summarized in Table 1. To investigate the effects of surface area and heterojunction on the photocatalytic activity, we normalized the reaction rate constants of the samples by surface area. Based on the N_2 adsorption–desorption isotherms, the BET surface areas (A_{BET}) of the samples were calculated, and are also summarized in Table 1. For pure g-C_3N_4, ng-CN has the highest BET surface area of 30.51 $m^2 g^{-1}$, but the normalized rate constant of ng-CN is the lowest. Thus, it can be concluded that the main reason for higher photocatalytic activity of ng-CN than that of mg-CN is its larger BET surface area. However, the normalized rate constants of the ng-CN/BiOCl heterojunction photocatalysts are higher than that of pure ng-CN, indicating that the heterojunction has an important effect on improving the photocatalytic activity. Among the ng-CN/BiOCl samples, the ng-CN/BOC-010 heterojunction photocatalyst shows the highest normalized rate constant, which is almost 2.3 times that of the ng-CN/BOC-001 heterojunction photocatalyst, suggesting that surface area is not a major factor influencing the photocatalytic efficiency of the composites.

Table 1. A_{BET}, k, and k′ of as-prepared g-C_3N_4, BiOCl, and g-C_3N_4/ BiOCl composites.

Samples	A_{BET} ($m^2 g^{-1}$)	k ($\times 10^{-3}$ min^{-1})	k'[a] ($\times 10^{-4}$ g $min^{-1} m^{-2}$)
mg-CN	13.21	1.32	1.00
mng-CN	21.74	2.05	0.94
ng-CN	30.51	2.69	0.88
mg-CN/BOC-001	8.07	1.23	1.52
mg-CN/BOC-010	9.35	1.21	1.30
mng-CN/BOC-001	14.47	4.05	2.80
mng-CN/BOC-010	15.62	8.37	5.36
ng-CN/BOC-001	16.03	6.95	4.34
ng-CN/BOC-010	18.10	18.38	10.16
BOC-001	2.21	0.35	—
BOC-010	4.69	0.78	—

[a] k' values are k values normalized by the surface areas.

Since MO is sensitive to visible light, its degradation is generally caused by a dye-sensitized path that does not require the band gap excitation of a photocatalyst. To demonstrate the visible-light-driven photocatalytic activity of the ng-CN/BiOCl heterojunction photocatalyst, phenol was chosen as a representative colorless organic pollutant for catalytic evaluation, as shown in Fig. 9b. The ng-CN/BiOCl heterojunction photocatalysts show superior catalytic performance, and the ng-CN/BOC-010 heterojunction photocatalyst exhibits higher photocatalytic activity than that of the ng-CN/BOC-001 sample. Fig. 9c shows the reaction constants of ng-CN/BiOCl heterojunctions containing different amounts of ng-CN. It is apparent that the highest photocatalytic efficiency is achieved for both ng-CN/BOC-001 and ng-CN/BOC-010 heterojunction photocatalysts as the proportion of ng-CN reaches 70 wt%. All the ng-CN/BOC-010 heterojunction photocatalysts show higher MO degradation rate constants than the corresponding ng-CN/BOC-001 samples.

The photostability of ng-CN/BiOCl heterojunction photocatalysts was also evaluated. High photocatalytic activity is maintained after six cycling runs, and there is no obvious catalytic deactivation, as shown in ESI Fig. S4, indicating the good stability of the ng-CN/BOC-001 and ng-CN/BOC-010 heterojunction photocatalysts. The ng-CN/BiOCl heterojunction photocatalysts after the degradation are examined by XRD, TEM and HRTEM (ESI Fig. S5). The XRD peaks of ng-CN/BiOCl show no detectable difference compared to the as-prepared ng-CN/BiOCl samples (Fig. 6a). As showed in ESI Fig. S5b and Fig. S5c, the crystal orientation of BiOCl are well maintained after the photocatalysis process.

Mechanism accounting for the photocatalytic activity enhancement in ng-CN/BiOCl heterojunction photocatalysts

Photoelectrochemical measurements were carried out to investigate the separation and migration of photogenerated charge carriers in the ng-CN/BiOCl heterojunction photocatalysts. The transient photocurrent responses of pure ng-CN, BiOCl, and ng-CN/BiOCl heterojunction photocatalysts are shown in Fig. 10a. The decay of the photocurrent indicates that a fraction of the holes recombine with electrons from the ng-CN conduction band instead of being trapped or captured by reduced species in the electrolyte. After recombination of the holes with electrons, the generation and transfer of electron–hole pairs reach a level of equilibrium and form a constant current, which has been clarified in a number of previous studies[53-55]. BOC-001 and BOC-010 show no obvious photocurrent owing to their large band gap. The enhanced photocurrent of ng-CN/BiOCl heterojunction photocatalysts compared to ng-CN indicates a more efficient separation and migration efficiency of the photoexcited electron–hole pairs. Also, the ng-CN/BOC-010 film electrode exhibits a higher photocurrent than that of the ng-CN/BOC-001 film electrode, indicating that the separation and migration efficiency of photogenerated electron–hole pairs depends on the exposed facets of the BiOCl substrate, and that BOC-010 favors the separation and migration of photogenerated electron–hole pairs. Fig. 10b shows the photoluminescence (PL) spectra of pure ng-CN, BiOCl, and the ng-CN/BiOCl heterojunction photocatalysts. The emission peak of ng-CN is centered at ca. 456 nm in the visible-light range, which is in good accordance with the band gap of ng-CN. Pure ng-CN displays the highest

intensity among these samples, which indicates that the charge carrier recombination in ng-CN is the fastest of the samples. The emission band positions of the ng-CN/BiOCl heterojunction photocatalysts are analogous to that of ng-CN, while the intensity of the ng-CN/BiOCl emission peaks is greatly weakened, indicating that the recombination of charge carriers is greatly suppressed and that the efficient separation of charge carriers is achieved. Moreover, the emission intensity of the ng-CN/BOC-010 heterojunction photocatalyst is significantly decreased compared to that of the ng-CN/BOC-001 sample, suggesting that the recombination rate of photogenerated charge carriers is lower in the ng-CN/BOC-010 heterojunction photocatalyst. The PL results are consistent with the transient photocurrent responses of the as-prepared samples.

To further investigate the charge transport performance of pure ng-CN, BiOCl, and the ng-CN/BiOCl heterojunction photocatalysts, electrochemical impedance spectroscopy (EIS) was used to investigate the charge carrier migration. As shown in Fig. 10c, the Nyquist plots of pure ng-CN, BiOCl, and the ng-CN/BOC heterojunction photocatalysts used as electrode materials cycled in 0.5 M Na_2SO_4 electrolyte solution show semicircles. The semicircle in the Nyquist plot can be simulated well by an electrical equivalent circuit model. In the model, the charge transfer resistance R_{ct} is in parallel with the double-layer capacitance (CPE), and the combination of R_t and CPE is in series with the total ohmic resistance of the electrolyte solution resistance R_s.[56] Since the preparation of the electrodes and electrolytes used are similar, the semicircle radius of the EIS plots are related to the resistance of the electrodes, further reflecting the efficiency of charge separation and transfer in these materials. A smaller semicircle radius, corresponding to a lower charge-transfer resistance value of R_{ct}, reflects higher electron−hole pair separation and transfer efficiency. ESI Table S1 shows the fitting results, which are calculated based on this model. It is apparent that the ng-CN/BiOCl heterojunction photocatalysts exhibit a much smaller semicircle radius and R_{ct} values than those of pure ng-CN, BOC-001, and BOC-010, demonstrating that the introduction of ng-CN into BiOCl can improve the separation and transport efficiency of photogenerated electron-hole pairs. Furthermore, the ng-CN/BOC-010 heterojunction photocatalyst shows a smaller semicircle radius with a lower R_{ct} value than that of the ng-CN/BOC-001 sample, suggesting that the ng-CN/BOC-010 heterojunction photocatalyst exhibits lower charge transfer resistance. The electrochemical measurements manifest that the exposed facet of BiOCl has an impact on the electron transport properties of ng-CN/BiOCl heterojunction photocatalysts.

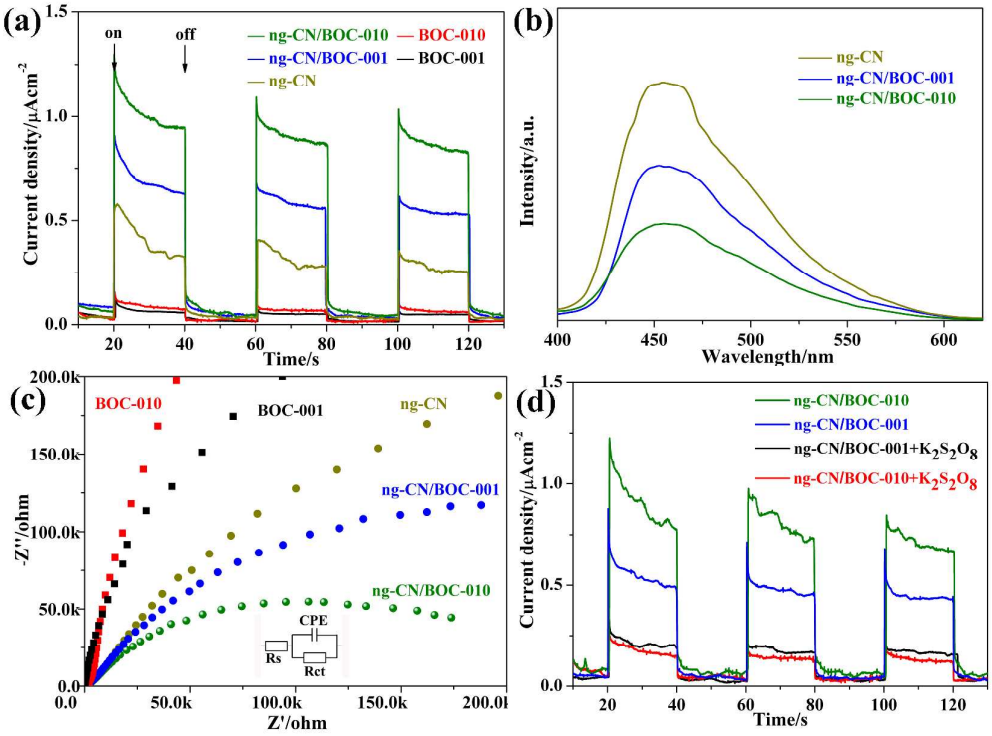

Fig. 10 (a) Transient photocurrent responses of pure ng-CN, BiOCl, and ng-CN/BOC heterojunction photocatalysts under visible-light irradiation (λ ≥ 420 nm) at 0.5 V vs. Ag/AgCl. (b) PL spectra of ng-CN and ng-CN/BiOCl heterojunction photocatalysts. (c) EIS Nyquist plots of ng-CN, BiOCl and ng-CN/BiOCl heterojunction photocatalysts. (d) Transient photocurrent responses of ng-CN/BOC-001 and ng-CN/BOC-010 heterojunction photocatalysts with and without the addition of $K_2S_2O_8$.

Fig. 11 displays the results of experiments involving the trapping of active species during reactions employing the ng-CN/BiOCl heterojunction photocatalysts. The photocatalytic degradation efficiency of ng-CN/BOC-001 and ng-CN/BOC-010 decrease to 49% and 78%, respectively, upon addition of TEOA, implying that photogenerated holes take part in the photocatalytic reactions. In addition, TBA as an •OH scavenger has no effect on the photodegradation of MO, suggesting that there is no •OH radical generated in the photocatalytic process. However, the photocatalytic degradation of MO is significantly decreased by the addition of $AgNO_3$, highlighting the crucial role of photogenerated electrons. The efficiency of MO removal is obviously inhibited by BQ, implying that $•O^{2-}$ is the main radical species in the degradation reaction. Therefore, it can be concluded that the degradation of MO over ng-CN/BiOCl samples is dominated by $•O^{2-}$ radicals, and involves the direct hole oxidation process to a lesser extent. The efficient separation and migration of electrons is a key to the photocatalytic activity.

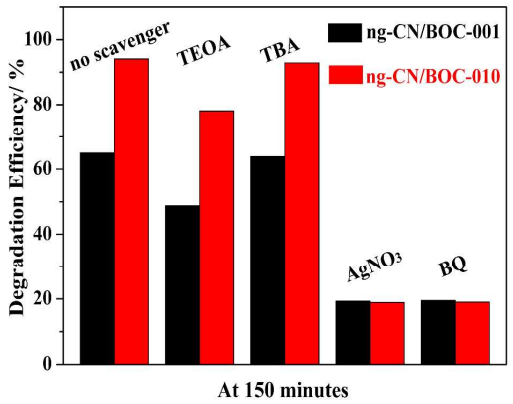

Fig. 11 Trapping of active species during the photodegradation of MO over ng-CN/BOC-001 and ng-CN/BOC-010 heterojunction photocatalysts under illumination by visible light for 150 min.

ESI Fig. S6 shows the valence band X-ray photoelectron spectroscopy (VB XPS) spectra of pure ng-CN, BOC-001, and BOC-010. The positions of the valence band edges of ng-CN, BOC-001, and BOC-010 are at ca. 1.44, 2.37, and 2.35 eV_{NHE} (NHE = normal hydrogen electrode), respectively. From UV–Vis diffuse-reflectance spectroscopy, BOC-001 and BOC-010 have similar band gap energies, which are estimated to be 3.41 and 3.42 eV, respectively. The band gap energy of pure ng-CN is a little larger than mg-CN, which can be assigned to a band gap of 2.72 eV. Based on above analyses, the energies of the conductance band (CB) edge of ng-CN, BOC-001, and BOC-010 are determined to be -1.28, -1.04, and -1.07 eV_{NHE}, respectively. As shown in Fig. 12, under visible-light irradiation (λ > 420 nm), ng-CN is easily excited and produces photogenerated electron–hole pairs, whereas BiOCl fails to produce any charges due to the wide band gap. Photogenerated electrons are prone to migrate from the CB of ng-CN to that of BiOCl since the E_{CB} of ng-CN is more negative than that of BiOCl, and then react with O_2 to produce $•O^{2-}$ radicals, which further contribute to degradation. Holes in the VB of ng-CN directly oxidize MO. Moreover, BOC-001 and BOC-010 have a similar band structure, and the energy band alignments are not obviously different between the ng-CN/BOC-001 and ng-CN/BOC-010 samples. The ng-CN/BOC-001 sample has a slightly larger CB offset (0.24 eV) than that of ng-CN/BOC-010 (0.21 eV). Therefore, the difference in photocatalytic performance between the ng-CN/BOC-001 and ng-CN/BOC-010 samples is not due to their conduction band offset.

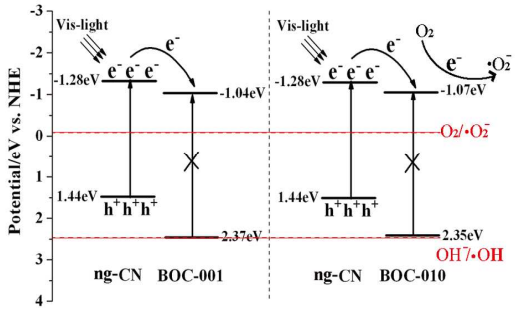

Fig. 12 Band alignments in ng-CN/BOC-001 and ng-CN/BOC-010 heterojunction photocatalysts.

Based on the above results, a proposed mechanism for the photocatalytic reactions occurring on the ng-CN/BOC-001 and ng-CN/BOC-010 heterojunction photocatalysts is presented in Fig. 13. The photocatalytic process consists of three steps: light absorption (steps A_1 and A_2), separation of electrons from ng-CN to the BiOCl surfaces (steps B_1 and B_2), and migration of the separated electrons to surface reactive sites (steps C_1 and C_2). Therefore, the photocatalytic activity of as-obtained heterojunctions can be described by Equation 1[57, 58]:

$$\eta = \eta_{LS} \times \eta_{CS} \times \eta_{CM} \quad (1)$$

where η can be expressed by photocurrent density (I), η_{LS} is the photon absorption rate, η_{CS} is the separation efficiency of electrons from ng-CN to the BiOCl surfaces, and η_{CM} is the migration of the separated electrons to surface reactive sites. UV-Vis DRS results demonstrate that the ng-CN/BOC-001 and ng-CN/BOC-010 heterojunction photocatalysts exhibit similar absorption of visible light. Thus, the photocurrent density (I) is a product of η_{CS} and η_{CM}:

$$I = \eta_{CS} \times \eta_{CM} \quad (2)$$

The charge carrier separation is mainly attributed to the conduction band offset in the ng-CN/BiOCl heterojunction photocatalyst; therefore, ng-CN/BOC-001 has a slightly larger η_{CS} value than ng-CN/BOC-010. This can be proved by transient photocurrent measurement with the addition of $K_2S_2O_8$ to eliminate the generated electrons (Fig. 10d). $K_2S_2O_8$ can consume the electrons that transfer from ng-CN to the BiOCl surfaces, and thus, steps C_1 and C_2 do not occur. With the

addition of $K_2S_2O_8$, the value of η_{CM} can be determined to be 1. Therefore, the photocurrent density is equal to η_{CS} only:

$$I = \eta_{CS} \quad (3)$$

As shown in Fig. 10d, the transient photocurrent intensity of ng-CN/BOC-001 becomes slightly higher than that of ng-CN/BOC-010 with the addition of $K_2S_2O_8$, indicating that ng-CN/BOC-001 has larger η_{CS} values than the ng-CN/BOC-010 sample. Therefore, the difference in photocatalytic activity is not caused by light absorption (steps A_1 and A_2, η_{LS}) or electron separation (steps B_1 and B_2, η_{CS}), but originates from the migration of the separated electrons to surface reactive sites (steps C_1 and C_2, η_{CM}). For the ng-CN/BOC-001 heterojunction photocatalyst, the internal electric fields in BOC-001 are perpendicular to the surfaces of BOC-001. Therefore, electrons arriving at the surface of BOC-001 prefer to transport within the BOC-001 bulk along the orientation of internal electric fields (process C_1 in Fig. 13). This leads to the waste of electrons during the long charge transport distance before reacting with O_2 to produce $\bullet O^{2-}$ radicals. However, the internal electric fields are parallel to the surfaces in BOC-010. Therefore, the preferred transfer orientation of separated electrons is along the surface of BOC-010 in the ng-CN/BOC-010 heterojunction. In this process, electron loss is significantly decreased due to the short charge transport distance, meaning that electrons can quickly react with O_2 to produce $\bullet O^{2-}$ radicals, which further contribute to degradation (process C_2 in Fig. 13). In other words, the ng-CN/BOC-010 heterojunction has a higher η_{CM} value than that of ng-CN/BOC-001. Therefore, it can be concluded that the internal electric fields of the supporting material BiOCl can determine the interfacial electron transport path and further affect photocatalytic performance. This mechanism explains the unusual crystal facet orientation-dependent photoactivity of g-C_3N_4/BiOCl composites. Calculations upon the first-principle theory are performed to reveal the band structures of BiOCl for obtaining the effective mass of electron along [001] and [010] direction (ESI Fig. S7). Based on the calculated results, the effective mass of electron along [001] and [010] direction are about 0.576 m_0 and 1.053 m_0 (m_0 is free-electron mass), respectively, indicating a higher mobility of electrons along [001] direction. These results suggest that separated electrons prefer to transport along [001] direction in BiOCl nanosheets. This means that the transfer of separated electrons is within the BOC-001 bulk in ng-CN/BOC-001, but along the BOC-010 surface in ng-CN/BOC-010. Nevertheless, more effort is needed to further clarify the underlying mechanism due to the complexity of heterojunctions in terms of composition and structure. At this stage, it is reasonable to conclude that the photocatalytic activities of the obtained g-C_3N_4/BiOCl photocatalysts are tuned by the orientation of the BiOCl nanosheets. The g-C_3N_4/BOC-010 heterojunctions are more active, which can be attributed to a cooperative effect of the built-in interface field and the lateral polar field afforded by the BOC-010 nanosheets.

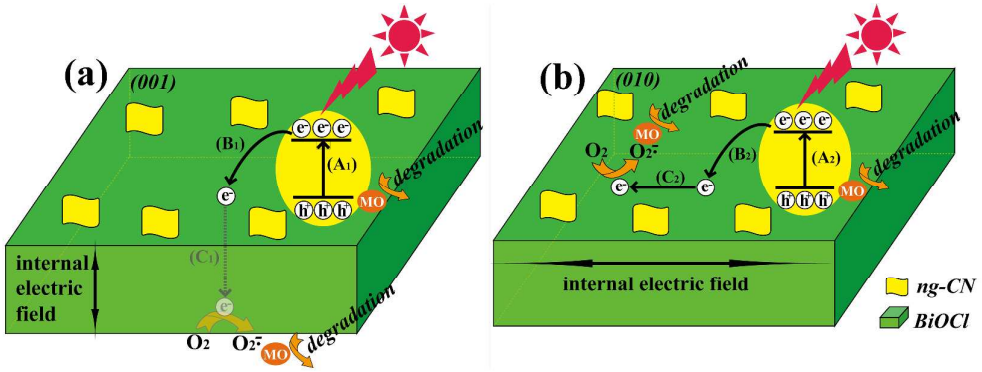

Fig. 13 Proposed mechanism for photocatalytic reactions occurring on ng-CN/BOC-001 and ng-CN/BOC-010 heterojunction photocatalysts.

Conclusions

In summary, size-controlled g-C_3N_4 was composited with different exposed facets of BiOCl. The results showed that ng-CN is uniformly deposited on the surface of BiOCl because good dispersity of ng-CN during sample preparation is beneficial to effective integration with BiOCl. Both the ng-CN/BOC-001 and ng-CN/BOC-010 heterojunction photocatalysts exhibited significantly enhanced MO and phenol photodegradation activity under visible-light irradiation. Also, the photocatalytic and photoelectrochemical behaviors of the ng-CN/BOC-001 and ng-CN/BOC-010 heterojunction photocatalysts were systematically compared and discussed, and it was demonstrated that the photocatalytic performance of ng-CN/BiOCl was affected by the internal electric fields in the BiOCl support. Owing to the internal static electric fields in the BiOCl substrate, electrons migrating from ng-CN to the surface of the BiOCl had a different transport path to the reactive sites. Photogenerated electrons had a shorter charge transport distance in BOC-010 than that in BOC-001, resulting in a lower electron loss before participating in reduction reactions. Thus, the ng-CN/BOC-010 photocatalyst showed higher photocatalytic activity than that of the ng-CN/BOC-001 photocatalyst.

Acknowledgements

This work was supported by the National Natural Science Foundation of China (Grant no. 21173131) and the Taishan Scholar Project of Shandong Province.

Notes and references

1. C. C. Wong and W. Chu, *Environ Sci Technol*, 2003, **37**, 2310-2316.
2. M. Li, X. F. Yu, S. Liang, X. N. Peng, Z. J. Yang, Y. L. Wang and Q. Q. Wang, *Adv Funct Mater*, 2011, **21**, 1788-1794.
3. T. B. Li, G. Chen, C. Zhou, Z. Y. Shen, R. C. Jin and J. X. Sun, *Dalton T*, 2011, **40**, 6751-6758.
4. K. H. Reddy, S. Martha and K. M. Parida, *Inorg Chem*, 2013, **52**, 6390-6401.
5. H. G. Kim, P. H. Borse, W. Y. Choi and J. S. Lee, *Angew. Chem.-Int. Edit.*, 2005, **44**, 4585-4589.
6. C. J. Li, P. Zhang, R. Lv, J. W. Lu, T. Wang, S. P. Wang, H. F. Wang and J. L. Gong, *Small*, 2013, **9**, 3951-3956.
7. J. S. Jang, H. G. Kim and J. S. Lee, *Catal. Today*, 2012, **185**, 270-277.
8. L. M. Sun, Y. Qi, C. J. Jia, Z. Jin and W. L. Fan, *Nanoscale*, 2014, **6**, 2649-2659.
9. P. Li, X. Zhao, C. J. Jia, H. G. Sun, L. M. Sun, X. F. Cheng, L. Liu and W. L. Fan, *J Mater Chem A*, 2013, **1**, 3421-3429.
10. L. Li, P. A. Salvador and G. S. Rohrer, *Nanoscale*, 2014, **6**, 24-42.
11. L. Q. Jiang, Y. H. Zhang, Y. Qiu and Z. G. Yi, *Rsc Adv*, 2014, **4**, 3165-3170.
12. T. P. Cao, Y. J. Li, C. H. Wang, C. L. Shao and Y. C. Liu, *Langmuir*, 2011, **27**, 2946-2952.
13. G. G. Briand and N. Burford, *Chem Rev*, 1999, **99**, 2601-2657.
14. S. X. Zhou, Y. X. Ke, J. M. Li and S. M. Lu, *Mater Lett*, 2003, **57**, 2053-2055.
15. S. J. Wu, C. Wang, Y. F. Cui, T. M. Wang, B. B. Huang, X. Y. Zhang, X. Y. Qin and P. Brault, *Mater Lett*, 2010, **64**, 115-118.
16. L. Chen, S. F. Yin, R. Huang, Y. Zhou, S. L. Luo and C. T. Au, *Catal Commun*, 2012, **23**, 54-57.
17. L. Q. Ye, L. Zan, L. H. Tian, T. Y. Peng and J. J. Zhang, *Chem Commun*, 2011, **47**, 6951-6953.
18. X. P. Lin, T. Huang, F. Q. Huang, W. D. Wang and J. L. Shi, *J Phys Chem B*, 2006, **110**, 24629-24634.
19. X. Zhang, Z. H. Ai, F. L. Jia and L. Z. Zhang, *J Phys Chem C*, 2008, **112**, 747-753.
20. K. L. Zhang, C. M. Liu, F. Q. Huang, C. Zheng and W. D. Wang, *Appl Catal B-Environ*, 2006, **68**, 125-129.
21. J. Jiang, K. Zhao, X. Y. Xiao and L. Z. Zhang, *J Am Chem Soc*, 2012, **134**, 4473-4476.
22. J. Cao, B. Y. Xu, H. L. Lin, B. D. Luo and S. F. Chen, *Catal Commun*, 2012, **26**, 204-208.
23. S. Shenawi-Khalil, V. Uvarov, E. Menes, I. Popov and Y. Sasson, *Appl Catal a-Gen*, 2012, **413**, 1-9.
24. W. J. Yang, B. Ma, W. C. Wang, Y. W. Wen, D. W. Zeng and B. Shan, *Phys Chem Chem Phys*, 2013, **15**, 19387-19394.
25. S. Y. Chai, Y. J. Kim, M. H. Jung, A. K. Chakraborty, D. Jung and W. I. Lee, *J Catal*, 2009, **262**, 144-149.
26. S. Shamaila, A. K. L. Sajjad, F. Chen and J. L. Zhang, *J Colloid Interf Sci*, 2011, **356**, 465-472.
27. F. Dong, Y. J. Sun, M. Fu, Z. B. Wu and S. C. Lee, *J Hazard Mater*, 2012, **219**, 26-34.
28. S. X. Weng, Z. X. Pei, Z. Y. Zheng, J. Hu and P. Liu, *Acs Appl Mater Inter*, 2013, **5**, 12380-12386.
29. L. M. Sun, L. Xiang, X. Zhao, C. J. Jia, J. Yang, Z. Jin, X. F. Cheng and W. L. Fan, *Acs Catalysis*, 2015, **5**, 3540-3551.
30. A. Thomas, A. Fischer, F. Goettmann, M. Antonietti, J. O. Muller, R. Schlogl and J. M. Carlsson, *J Mater Chem*, 2008, **18**, 4893-4908.
31. K. Maeda, X. C. Wang, Y. Nishihara, D. L. Lu, M. Antonietti and K. Domen, *J Phys Chem C*, 2009, **113**, 4940-4947.
32. X. C. Wang, K. Maeda, X. F. Chen, K. Takanabe, K. Domen, Y. D. Hou, X. Z. Fu and M. Antonietti, *J Am Chem Soc*, 2009, **131**, 1680-+.
33. X. C. Wang, K. Maeda, A. Thomas, K. Takanabe, G. Xin, J. M. Carlsson, K. Domen and M. Antonietti, *Nat Mater*, 2009, **8**, 76-80.
34. S. Martha, A. Nashim and K. M. Parida, *J Mater Chem A*, 2013, **1**, 7816-7824.
35. S. C. Yan, Z. S. Li and Z. G. Zou, *Langmuir*, 2010, **26**, 3894-3901.
36. S. C. Yan, Z. S. Li and Z. G. Zou, *Langmuir*, 2009, **25**, 10397-10401.
37. P. Niu, G. Liu and H. M. Cheng, *J Phys Chem C*, 2012, **116**, 11013-11018.
38. C. C. Han, L. Ge, C. F. Chen, Y. J. Li, X. L. Xiao, Y. N. Zhang and L. L. Guo, *Appl Catal B-Environ*, 2014, **147**, 546-553.
39. L. Ge, C. C. Han and J. Liu, *Appl Catal B-Environ*, 2011, **108**, 100-107.
40. H. Xu, J. Yan, Y. G. Xu, Y. H. Song, H. M. Li, J. X. Xia, C. J. Huang and H. L. Wan, *Appl Catal B-Environ*, 2013, **129**, 182-193.
41. X. D. Zhang, X. Xie, H. Wang, J. J. Zhang, B. C. Pan and Y. Xie, *J Am Chem Soc*, 2013, **135**, 18-21.
42. Alicja Mikolajczyk, Agnieszka Gajewicz, Bakhtiyor Rasulev, Nicole Schaeublin, Elisabeth Maurer-Gardner, Saber Hussain, Jerzy Leszczynski and T. Puzyn, *Chemistry of Materials*, 2015.
43. C. Ribeiro, E. Longo and E. R. Leite, *Appl Phys Lett*, 2007, **91**.
44. V. R. de Mendonca, C. J. Dalmaschio, E. R. Leite, M. Niederberger and C. Ribeiro, *J Mater Chem A*, 2015, **3**, 2216-2225.
45. T. Hawa and M. R. Zachariah, *J Aerosol Sci*, 2006, **37**, 1-15.
46. P. Niu, L. L. Zhang, G. Liu and H. M. Cheng, *Adv Funct Mater*, 2012, **22**, 4763-4770.
47. M. Groenewolt and M. Antonietti, *Adv Mater*, 2005, **17**, 1789-+.
48. X. J. Wang, Q. Wang, F. T. Li, W. Y. Yang, Y. Zhao, Y. J. Hao and S. J. Liu, *Chem Eng J*, 2013, **234**, 361-371.
49. F. Chang, Y. C. Xie, J. Zhang, J. Chen, C. L. Li, J. Wang, J. R. Luo, B. Q. Deng and X. F. Hu, *Rsc Adv*, 2014, **4**, 28519-28528.
50. L. Armelao, G. Bottaro, C. Maccato and E. Tondello, *Dalton T*, 2012, **41**, 5480-5485.
51. S. P. Wang, C. J. Li, T. Wang, P. Zhang, A. Li and J. L. Gong, *J Mater Chem A*, 2014, **2**, 2885-2890.
52. G. Liu, P. Niu, C. H. Sun, S. C. Smith, Z. G. Chen, G. Q. Lu and H. M. Cheng, *J Am Chem Soc*, 2010, **132**, 11642-11648.

53. J. G. Yu, Y. Wang and W. Xiao, *J Mater Chem A*, 2013, **1**, 10727-10735.
54. G. P. Dai, J. G. Yu and G. Liu, *J Phys Chem C*, 2011, **115**, 7339-7346.
55. J. G. Yu and B. Wang, *Appl Catal B-Environ*, 2010, **94**, 295-302.
56. W. J. Jo, J. W. Jang, K. J. Kong, H. J. Kang, J. Y. Kim, H. Jun, K. P. S. Parmar and J. S. Lee, *Angew. Chem.-Int. Edit.*, 2012, **51**, 3147-3151.
57. F. F. Abdi, N. Firet and R. van de Krol, *Chemcatchem*, 2013, **5**, 490-496.
58. H. Dotan, K. Sivula, M. Gratzel, A. Rothschild and S. C. Warren, *Energ Environ Sci*, 2011, **4**, 958-964.